Publications of the Astronomical Society of the Pacific
105: 731–747, 1993 July

Full-orbit H-alpha Emission in RW Tauri

David N. Vesper and R. Kent Honeycutt
Indiana University, Department of Astronomy, Swain Hall West 319, Bloomington, Indiana 47405
Electronic mail: vesper@indiana.edu,honey@indiana.edu

Received 1993 March 5; accepted 1993 April 13

ABSTRACT. Hα observations of the Algol system RW Tauri were obtained over a four-year period (1988 October–1992 September) at $\sim$1 Å resolution, with coverage over the full orbit. Strong single-peaked emission near orbital quadrature is easily seen in the raw spectra. Subtracting the stellar components' light reveals a second, weaker, often double-peaked emission component at almost all phases, at most epochs. An absorption component is seen just before and after primary eclipse. Visibility and velocities for the strong emission place it between the stellar components, near the primary star. Depending on the epoch, this stronger emission has one of two distinct patterns in a velocity versus phase plot. The weaker emission feature's visibility and velocity indicate that it usually arises from a slowly rotating structure near the primary star, with a radial extent of at least 0.33 R_1. A third feature (which we interpret as a transient ring) was present in 3 of 12 runs.

1. INTRODUCTION

Algols are close, interacting binaries in which mass transfer occurs as a result of Roche-lobe overflow from the secondary (cooler) star. The accretion structures arising from the mass transfer often give rise to emission lines. Permanent Hα emission from accretion disks has been observed in many long-period Algols (Peters 1989 and references therein). Transient Hα in-eclipse emission has also been observed in several short-period ($\lesssim$5 days) Algols, and has been the subject of several studies (Kaitchuck et al. 1985 and references therein). There have been occasional reports of out-of-eclipse emission in the short-period systems. Examples include Beta Per (Struve and Sahade 1956), U CrB (Struve et al. 1957), TX UMa (Plavec and Polidan 1976), and TZ Eri (Peters 1989). Only recently has out-of-eclipse emission been the subject of any extensive studies, and these studies have been limited to Algol itself (Gillet et al. 1989; Richards 1992,1993) and a preliminary report on RW Tauri (Honeycutt et al. 1993).

We have been conducting an ongoing program to survey out-of-eclipse Hα emission in short-period Algols. The survey has two parts. RW Tau is one of a few Algols to receive full-orbit coverage over several years. About 40 additional systems are being observed only near orbital quadrature, where the emission is most prevalent. These data will allow a detailed study of the emission's characteristics and long-term variability.

RW Tau is a totally eclipsing Algol, with the deepest known primary minimum (exceeding 5 magnitudes in the ultraviolet). Table 1 summarizes data on the system. RW Tau has a long history of spectroscopically observed Hα emission, mostly in eclipse (Kaitchuck and Honeycutt 1982 and references therein; hereafter referred to as KH).

2. OBSERVATIONS

Hα spectra of these Algols are obtained with the Indiana CCD spectrograph mounted on the 102-cm reflector at the U.S. Naval Observatory, Flagstaff Station. To date, there have been twelve observing runs of varying length. The eleven runs which included RW Tau observations are summarized in Table 2. There are 92 good exposures of RW Tau, scattered over the system's orbit. A typical exposure has a spectral resolution of $\sim$1 Å over the wavelength range 6400–6700 Å. This paper primarily examines the 73 exposures obtained outside primary eclipse. Unless otherwise specified, these will be referred to as "out-of-eclipse" data, even though we include data during the secondary eclipse. The out-of-eclipse observations had a typical exposure time of 20 min (or $\sim$0.005 phase units). Five observations are also presented from the totality of primary eclipse. The 14 exposures taken during the partial phases of primary eclipse will not be examined, primarily due to the difficulty in modeling the stellar spectra during these phases. We will refer to individual observations with a "rr-nnn" format, meaning the "nnn$^{\text{th}}$" image of the "rr$^{\text{th}}$" observing run. Since many objects other than RW Tau are examined during each run, there are gaps in these numbers.

3. REDUCTIONS

We used a quartz lamp for flat fields and a neon lamp for wavelength calibration. The initial reductions were done with the IRAF CCDRED package. All spectra were normalized to a continuum of unity. To examine the Hα emission in detail, it is necessary to isolate the emission from the stellar component's light. To this end, a model of the stellar components' spectral profile was created. This was fitted to the wings of the observations and subtracted. The resulting "difference profile" can then be studied.

Since RW Tau has undergone several period changes (mainly decreases) in the past (Frieboes-Conde and Herczeg 1973; Kholopov 1985), it was necessary to determine an updated ephemeris that covered the epochs of the observations. Table 3 summarizes times of minimum light near the beginning and end of the observation period, as well as a reference ephemeris (Kholopov 1985). The last

TABLE 1
RW Tau Data

a) System Properties

		Ref.
γ_{vel} (km s^{-1})	-20.2	a
K_{vel} (km s^{-1})	53	a
P (days)	2.76876	e
Mass ratio (q)	0.2258	c
i (degrees)	90	c
$a \sin i$ ($R_\odot$)	15.8	c

b) Component Properties

	Primary	Secondary	Ref.
Spec Type	B8V	K0IV	a
Mass ($M_\odot$)	2.43	0.55	d
Radius ($R_\odot$)	2.97	...	c
$T_{\rm eff}$ (K)	11,750	4270	d
$\log(g_{\rm eff})$	3.85	...	e
$v \sin i$ (km s^{-1})	94	88	d,e
Limb dark coeff	.37	.6	b

References:

a Batten et al 1989
b Grygar et al 1972
c Terrell et al 1992
d Van Hamme & Wilson 1990
e This paper

four minima were observed with the IU CCD-Automated Photometric Telescope (Honeycutt et al. 1990; Honeycutt and Turner 1993). Of these four, the first two were of third contact only. Their Julian Date assumes their duration of totality was equal to that of the latter eclipses. The first $O-C$ values make clear that a period change occurred between 1983 and 1988 (the beginning of our observing program), and that changes continued through 1992. The linear ephemeris adopted for the minima during this observing program is

$$Min\ \mathrm{I(HJD)} = 2447525.4486 + 2.76876\ \mathrm{E} \pm 0.00001.$$

The $O-C$ values for this ephemeris are also given in Table 3. The largest $O-C$ translates to an 0.0009 phase error ($\sim 1/6$ the exposure duration). A more detailed analysis of the period changes will appear at a later date.

TABLE 2
Observing Run Summary

Observing Run Number[a]	UT Dates	Number of RW Tau Obs[b]
1	1988 Sep 08–13	4
2	1988 Oct 29–Nov 02	9
3	1989 Jan 29–Feb 01	6(2)
5	1989 Dec 15–22	12(3)
6	1990 Nov 14	2
7	1991 Feb 04–10	8
8	1991 Sep 12–17	8
9	1991 Oct 15–20	6
10	1991 Dec 13–17	6
11	1992 Sep 05–10	10
12	1992 Dec 11–15	2

Notes: [a] We have listed only the runs in which RW Tau was observed.
[b] Number of out-of-eclipse observations, followed in parentheses by number during the totality of primary eclipse.

TABLE 3
Times of Minima for RW Tau

UT Date	Julian Date	$O-C^a$ (days)	$O-C^b$ (days)	Ref
1983 Dec 15	45684.204	...	...	c
1988 Dec 29	47525.4486	-0.031	...	d
1991 Oct 23	48552.661	-0.057	+0.002	e
1992 Oct 14	48909.830	-0.067	+0.001	e
1992 Oct 25	48920.904	-0.069	+0.001	e
1992 Oct 28	48923.674	-0.068	+0.002	e

Notes: [a] With respect to the ephemeris in Kholopov 1985
[b] With respect to the ephemeris in this paper

References:

c Kholopov 1985
d Hanžl 1990
e This paper

However, it is worth noting that this new period represents the largest period change in RW Tau since the early 1900s, with a $\Delta P/P$ of -3×10^{-5}.

4. CREATION OF THE DIFFERENCE PROFILES

To examine the out-of-eclipse spectra, a synthetic line profile for the stellar components is needed. There have been several reports over the years that RW Tau has an (optical?) companion $\sim 1''$ away (Joy 1942; Frieboes-Conde and Herczeg 1973; Chambliss 1992). The companion is reported to have $V=12.5$. This star should have been visible to us in our guiding camera as a distortion of RW Tau's seeing disk, but such a distortion was not seen. This star would produce $\sim$40% of the total light during primary minimum. We would expect the spectral lines of this companion to be visible in the eclipse spectra. KH did not report seeing any anomalous lines during the 18 eclipses they observed. While we do not doubt the existence of this third star, there is insufficient information about this body for us to include it in our synthetic system spectra. Instead we will treat the in-eclipse light as arising solely from the system's secondary star. For the V magnitude above, we can estimate that the third component will contribute $\sim$2% of the system's out-of-eclipse light at Hα. Any error generated by ignoring this star is smaller than the errors we quote in Sec. 4.2 for our reduction technique.

4.1 Creation of the Synthetic Spectra

The model spectra consist of two parts, the B star and the K star. The B star's model is formed from a Kurucz (1979) model atmosphere line profile. Specifying the Hα profile requires the effective temperature and effective gravity. A solar abundance is assumed. Kurucz calculated the models at steps of 1000 K in $T_{\rm eff}$ and 0.5 in $\log(g)$. Bilinear interpolation between models allows approximations to profiles at other $T_{\rm eff}$ and $\log(g)$ values. Van Hamme and Wilson's (1990) analysis of photometry of RW Tau gives $T_{\rm eff}$= 11,750. Plavec and Dobias's (1983) UV-visible-IR continuum fit of RW Tau to the Kurucz models gives a

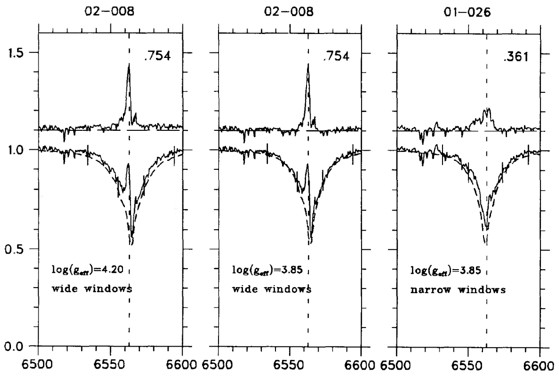

FIG. 1—Examples of different $\log(g_{\rm eff})$ and different windows sizes for the wavelength calibration fit. Each box contains the following features: (a) the observed spectrum is a solid line, normalized to a continuum of unity, (b) the synthetic spectrum is a dashed line, normalized to a continuum of unity, (c) the difference profile is a solid line, shifted up 0.1 for clarity, (d) the vertical dashed line is the wavelength of Hα in the CM frame, (e) the horizontal dashed line is the continuum for the difference profile, (f) the vertical tics on the Hα wings mark the wing fit windows, (g) the phase is in the box's upper right-hand corner, and (g) the image's name is above each box. The first image has a synthetic B-star profile with a $\log(g_{\rm eff})=4.20$. The second is the same observation with a $\log(g_{\rm eff})=3.85$ synthetic B-star profile. Both use the wide windows. The third spectrum is an example of poorly fitted data. It uses the narrower windows.

$T_{\rm eff}=11{,}750$ and $\log(g)=4.2$ model. We adopted $T_{\rm eff}=11{,}750$. However, a calculation of the effective gravity from the stellar parameters in Table 1 gives $\log(g_{\rm eff})=3.85$. As a check, profiles using both values of $\log(g_{\rm eff})$ were plotted versus the observed profiles. The first two panels of Fig. 1 shows that $\log(g_{\rm eff})=3.85$ is better. This is not unreasonable since we expect a fit to the wings of a line profile to be a more sensitive measure of the effective gravity than a fit to a continuum. Once a profile is chosen, it is convolved with a limb darkening and rotation profile (Gray 1976) to match the primary star (see Table 1 for rotation and limb darkening parameters).

Since the K star's spectral type has many lines near Hα, a field star spectrum (HR 8857, K0 IV) obtained with the same instrument was used rather than a model. While HR 8857 has some rotation, it is small compared to the (assumed) synchronous $v\sin(i)=88$ km s^{-1} of RW Tau's secondary. Therefore the field star spectrum was also convolved with a limb darkening and rotation profile (see Table 1 for parameters).

To scale the relative intensities of the stellar spectra, a magnitude difference at Hα is needed. This is calculated as follows:

$$\Delta {\rm H}\alpha=({\rm H}\alpha_{\rm K}-{\rm V}_{\rm K})-({\rm H}\alpha_{\rm B}-{\rm V}_{\rm B})+\Delta {\rm V}$$

where the subscripts B and K refer to the B star and K star, respectively, and ΔHα and ΔV are the difference in magnitudes at Hα and the V band, respectively. Using $({\rm H}\alpha_{\rm B}-{\rm V}_{\rm B})=0.20$ and ${\rm H}\alpha_{\rm K}-{\rm V}_{\rm K}=-0.44$ (Gunn and Stryker 1983), we converted the magnitude difference to a luminosity ratio. This results in scaling the stellar spectra models so the primary emitted 94% of the system's light at Hα.

For each out-of-eclipse observation (excluding secondary eclipse), the synthetic spectra were Doppler shifted to match the appropriate phase, and added to form a model of the system's stellar light at Hα. Finally, the combined profile is convolved by the instrument profile (a Gaussian of $\sigma=0.37$ Å).

During secondary eclipse, the process is more complicated. Each components' rotation profile, limb darkening effects, and intensity are affected by their relative visibility. In this case the composite profile is created by placing a grid over the stars in the geometry of the particular phase. The grid size was chosen to assure an accuracy of 0.02 Å for the rotation profile. At each point the intensity from the "raw" (nonrotated and nonlimb darkened) synthetic stellar spectra is modified by the grid's velocity and limb darkening coefficient. Summing over the whole grid gives the profile.

For these synthetic spectra the reflection effect and gravity darkening were ignored. These effects are only significant during the partial phases of primary eclipse (where we are not examining data). For visibility, limb darkening, and rotation effects, both stars were modeled as triaxial ellipsoids. Since only the very faint K star has any significant Roche geometry and it contributes very little to the observed profile, this should not degrade the results.

4.2 Fitting the Synthetic Spectra to the System Spectra

At this point, the expected procedure would be to shift the composite model spectra and the observed spectra into a common velocity frame and subtract them. However, the wavelength calibration of the spectra is not as good as would be desired. To improve the wavelength match, an alternate method was used. If the wings of the Hα profile can be assumed to be uncontaminated with nonstellar emission, then a fit to these wings should give the location of Hα (and hence a wavelength zero-point) in the B-star's rest frame. The wavelength dispersion is still determined from the neon calibration spectra. The actual wing fit used a cross-correlation/lag technique. The synthetic spectrum is lagged in ∼0.04 Å intervals over a suitably large range. The lag is found that minimizes the difference in the observed and synthetic profile. This difference is calculated in two windows centered on Hα. The choice in window sizes and locations is constrained by the need to avoid contaminated areas, and at the same time to maximize the use of available data. After experimentation, two sets of windows were used. All but three runs used windows that spanned the interval 9–30 Å above and below Hα. For runs 1, 7, and 10, the emission contaminated these windows and we used a narrower set that covered the interval 12–30 Å above and below Hα. These windows are displayed in Fig. 1.

The windows need to be centered on Hα in the B-star's frame, but this is initially unknown. Therefore an iterative procedure was used. First, the windows were placed using the observed wavelength calibration. This was used to find an approximate B-star rest frame, and this frame was used to find a new wavelength calibration. A new pair of win-

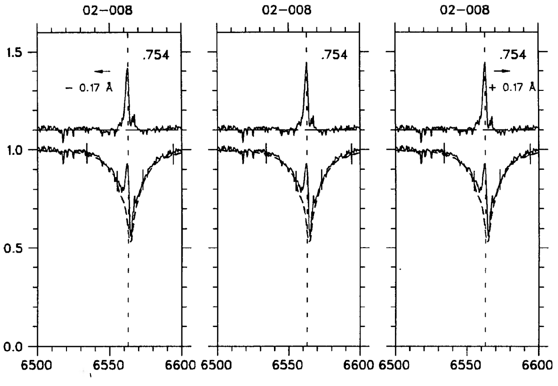

FIG. 2—An example of intentionally misaligned observed/synthetic spectra. The format for each spectrum is the same as Fig. 1. The center spectrum used the calculated lag fit. In the left spectrum the synthetic spectrum was intentionally blueshifted 0.17 Å before subtraction from the observed spectrum. In the right spectrum the synthetic spectrum was intentionally red shifted 0.17 Å before subtraction from the observed spectrum. The parameters of the difference profile emission features are shown in Table 4. Note the small red-shifted emission spike in the observed spectra, corresponding to the weaker emission feature in the difference spectra.

dows were calculated and another cross correlation/lag performed. The process was repeated until the wavelength calibration (and window location) stabilized. Now that the synthetic and object spectra are in the same rest frame, they are subtracted. The resulting spectrum (called a difference profile) should show the nonstellar emission components of the system. Figure 1 gives three examples of the synthetic spectra fit and resulting emission spectra.

A measure of the final wavelength accuracy was obtained from pairs of RW Tau spectra taken in rapid sequence. The standard deviation of the wavelength zeropoint is 0.17 Å ($\sim$8 km s^{-1}). Figure 2 gives examples of spectra that were intentionally misaligned by plus or minus this standard deviation. The appearances of the resulting profiles are scarcely different. Table 4 shows the sensitivity of the radial velocities and equivalent widths (EWs) to the misalignments. These values are representative of those found when other spectra are intentionally misaligned. From these values, we may infer an internal accuracy of $\sim$0.05 Å and $\sim$5 km s^{-1} in EW and radial velocity, respectively, due to the cross-correlation/lag process. Another measure can be made for the external errors from the nightly presence of telluric water vapor lines. These lines contaminate the blue-shifted cross-correlation/lag window. As a test, the telluric features were removed from observation 02-008 by hand. The new spectrum produced a best fit that was -0.20 Å from the fit of the observed spectrum. The last line in Table 4 lists the EWs and radial velocities for the emission features for this fit. The errors are similar to the internal cross-correlation/lag errors quoted above. This indicates the external cross-correlation/lag errors (between observing runs) should be taken to be slightly larger than the internal error quoted above.

TABLE 4

Emission Data for Error Measures

Shift	Strong		Weak	
	EW Å	Velocity km s^{-1}	EW Å	Velocity km s^{-1}
+0.17[a] Å	1.13	-56	0.11	+160
0.0 Å	1.09	-62	0.15	+154
-0.17[a] Å	1.03	-68	0.18	+152
-0.20[b] Å	1.03	-69	0.19	+149

Notes: [a] One standard deviation of the wavelength error.
[b] The external error contribution from telluric water vapor lines.

4.3 In-Eclipse Observations

For observations taken during the totality of primary eclipse we need only remove the spectra of the K star. Once again, HR 8857 was used after convolution with a rotation profile. Because the Hα wings of this late-type star are not free of other features, the wing fit technique does not work. Instead, we were able to take advantage of the numerous other lines in the spectra. A least-squares fit was performed to minimize the differences in wavelength between the RW Tau eclipse spectrum and the HR 8857 absorption spectrum, excluding Hα. This fixed the wavelength zeropoint. The dispersion is still fixed by the neon lamp calibration spectra. The standard star was then shifted to match the wavelength scale of each eclipse spectrum and subtracted.

5. ANALYSIS OF THE DIFFERENCE PROFILES

5.1 Out-of-Eclipse Profiles

The out-of-eclipse emission spectra are displayed in Fig. 3. Several facts are readily noted. Some emission is present at all phases except those near primary eclipse. The emission is usually double peaked and strongest near orbital quadratures. Near phase 0.25 the strongest emission component is red shifted and sharply peaked. At this phase the weaker component is blue shifted, sharply peaked, and often much weaker than the red-shifted component. Near phase 0.75, the situation is usually similar, but with the Doppler shifts reversed. Near phase 0.5 the emission always has two peaks, both about the same strength as the weaker quadrature peaks. Absorption is seen just before and after primary eclipse, sometimes with emission superimposed.

The strength of the emission varies on a time scale of weeks. While there are variations between all observing runs, it is worth noting here the particularly anomalous behavior during runs 1, 7, and 10. The normally weak and sharp secondary peak is broad and as strong or stronger than the normally strong peak. The match between the observed and synthetic wings also varies with each run. The synthetic wings are too low in run 1. They are also low (but not as much) in runs 3, 7, 10, and 11. Runs 2 and 5 have some low synthetic wings and some very good matches. Runs 6, 8, and 9 all have excellent matches. Finally, there are a few spectra where the synthetic wings are too high (mainly in run 2). These variations are probably related to difficulties in fitting the continuum in the region of a very wide absorption feature, in data that is not noise-free. Observation 01-026 has a wide emission component that is exaggerated by the wing mismatches (see Fig. 1). This is a good example of how small features in the data are magnified when two sloping lines are subtracted. This observation shows the best examples of these problems and makes it clear that care must be taken in examining features in the spectra. There must therefore be some questions of the reality of the weaker features. For now, the fact

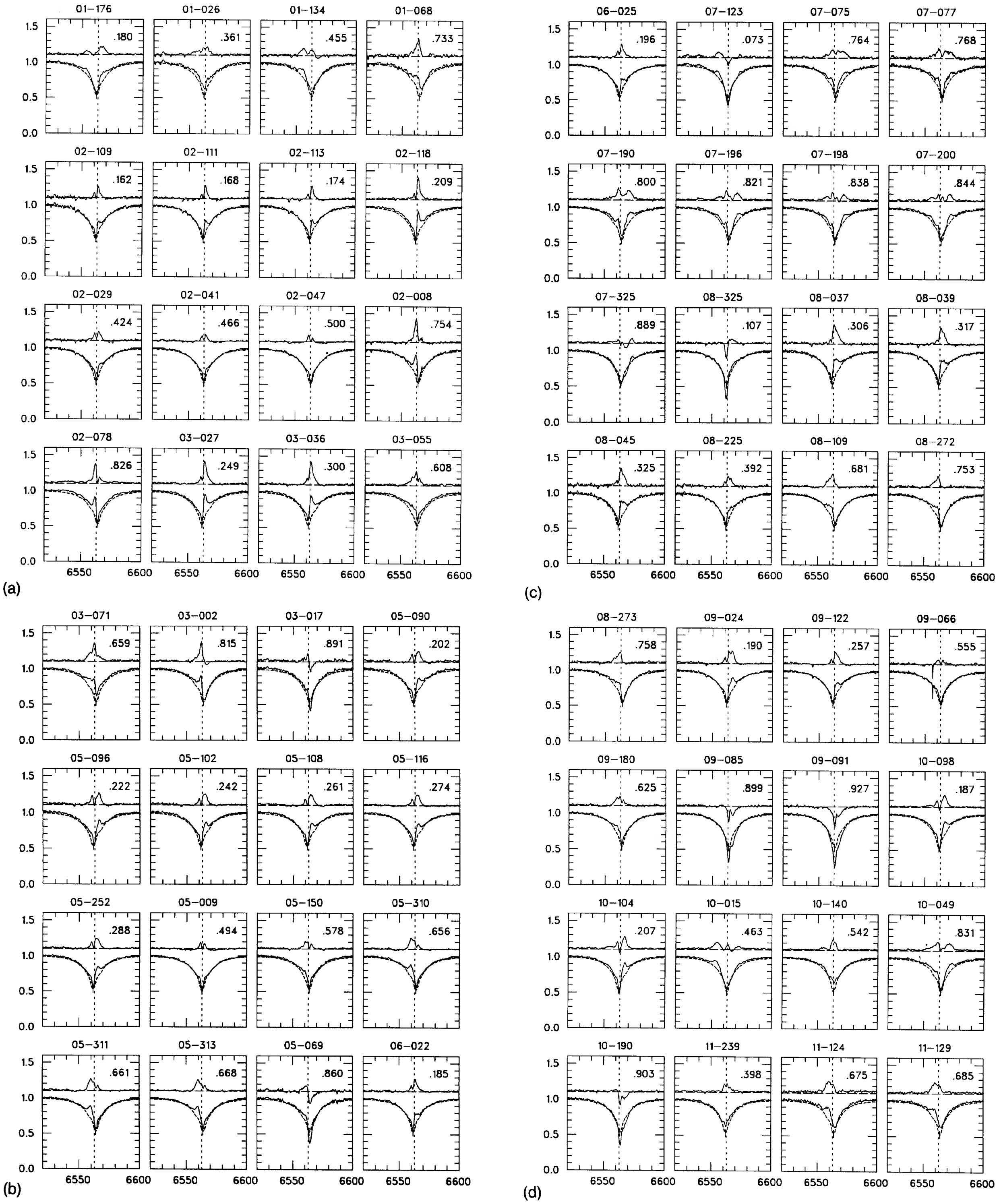

FIG. 3—(a) The observed, synthetic, and difference profiles for all the observations. The format for each spectrum is the same as in Fig. 1 except the wing fit windows are not displayed. The wavelength scale is listed at the bottom of the plot. The spectra are arranged by observing run, and by phase within each run. (b)–(e) Same as (a).

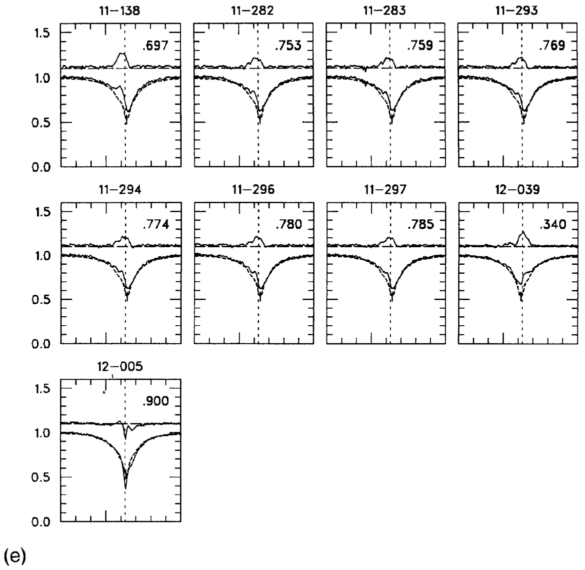

FIG. 3—(Continued)

that in many of the observed spectra a small secondary spike can be seen will be taken to indicate its reality (see Fig. 2).

5.2 Equivalent Widths and Velocities

The IRAF task SPLOT was used to measure equivalent widths (EWs) and mean radial velocities for the emission features in the difference profiles. Their values are listed in Table 5. At all phases the EWs are with respect to the continuum as seen outside of eclipse. Velocities are listed in the system center-of-mass (CM) rest frame and the B-star rest frame. Unless otherwise specified, we will use the CM rest frame velocities in the following discussions.

The EW and velocity were generally found by direct integration of the emission intensity at each pixel. However, during two runs (2 and 6) the strong emission sources always have a near-Gaussian shape. For these runs only, the strong emission features' EWs and velocities were found by fitting a Gaussian curve. This was done primarily to increase the accuracy of the velocities. As can be seen in Fig. 2, the blue wings of the strong feature are wider than we would expect from a Gaussian shape. This may be an artifact of the synthetic spectra subtraction or due to an additional emission source. In any event, we feel that the strong feature emission source is best represented by the Gaussian portion of the feature. While we would like to similarly isolate individual emission features in every difference profile, their nonuniform shape and our lack of fore knowledge of the emission sources makes this impossible. Likewise, we are tempted to fit Gaussians to the few strong emission features in run 3 that have near-Gaussian shapes. However, we feel it is important to maintain consistency within each observing run. Since not all the strong features in run 3 have Gaussian shapes, we did not fit any of them with Gaussians. In any event, for runs 2 and 6 the Gaussian fit EWs are the same (to within our errors) as those from direct integration of pixel intensities, while the Gaussian velocity magnitudes are ~ 30 km s^{-1} smaller than the direct integration values. In our later discussion of the emission sources, we will remain alert for any systematic differences in the EWs and velocities of these runs that might arise from the different reduction technique.

As mentioned above, examining the EWs and velocities is complicated by the possibility of several emission sources, and by the variation in behavior between epochs. Ideally, the data for each emission source would be plotted separately. For now, the data will be divided into two groups. "Type A" emission will be used to refer to the strong component that is red shifted near phase 0.25, blue shifted near phase 0.75, and not visible during or near the eclipses. This is the peak that is visible in the raw spectra and dominates most of the emission spectra. For runs 2 and 6 this emission was fit with Gaussian curves. "Type B" emission refers to all other emission components, including the usually weaker component near quadrature, both components of double-peaked emission near phase 0.5, and the strongest emission during run 7. The distinction between the two categories is not exact, and there are transitional points (especially around the eclipse).

Figure 4 shows the EWs and velocities of the Type A emission. The EWs show that emission appears to be absent in the phases surrounding primary and secondary eclipses. While this partially follows from our definition of Type A emission features, the decline in the strength of the emission as the eclipses are approached (in runs 2, 7, and 11) shows this to be a real feature of the emission. Further, the Type B emission features which remain in the phase interval 0.4–0.6 mostly have EWs$\lesssim$0.3 Å [see Fig. 5(a)]. The data from run 11 indicate a peak near phase 0.75, while the data from runs 5 and 10 remain constant (or decrease) from phase 0.2 to 0.3. The other runs do not give a clear indication of their peak.

The velocity data are more complicated. The velocities from phase 0.15 to 0.45 appear to separate into two groups. One group (runs 2 and 6) has a velocity of about 20 km s^{-1} near phase 0.15. The other group (runs 3, 5, 8, and 9) drops from 130 km s^{-1} at phase 0.2 to 60 km s^{-1} at phase 0.3. Near phase 0.4 two points match the velocities of the Type B emission (as seen below). The point near phase 0.36 is from observation 01-026, which has already been mentioned to have a poor synthetic/observed spectral profile fit. From phase 0.65 to 0.85 the magnitude of the velocity of the Type A emission varies with each run. For runs 2, 3, and 8 the velocity magnitude remains constant or increases, while for runs 7 and 11 it decreases. The run 10 observation at phase 0.83 stands out with an exceptionally large velocity. This is probably a result of the poor fit between the wings of the synthetic and system spectra in the observation.

Figure 5 shows the Type B emission data. The EW generally varies from 0.1 to 0.4 Å, with little systematic phase dependence. Observations where no Type B emission was detected are marked by points of 0.05 Å (the lower limit of detection) and a downward pointing arrow. Points near phases 0.0 and 1.0 are for in-eclipse data, and will be discussed later. Figure 5(a) shows a few nondetections scattered in phase and a large cluster near phase 0.75. Most of these are from run 11 where all the observations were near 0.75. However, runs 3 and 8 show Type B emission at phases less than 0.68, but none afterwards. Figure 5(b) shows that most runs have velocity magnitudes about 100 km s^{-1} larger than the B star at all phases from 0.15 to 0.85. This strongly suggests a ring of material on or around the B star.

Type B emission from runs 1, 7, and 10 deserve special mention. These all have exceptionally strong EWs. At phase 0.8 the run 7 EW is 0.9 Å, and it drops dramatically to 0.2 Å by phase 0.9. The run 7 velocities increase from 260 to 440 km s^{-1} in the phase range 0.78–0.89. Runs 1, 7, and 10 mostly have emission with high maximum velocities of ~ ±400 km s^{-1}, well above the 135–150 km s^{-1} the other runs consistently showed. Also, runs 1 and 10 have nearly-at-rest emission near phase 0.5 and run 7 has nearly-at-rest emission near phase 0.85. Because of the similarity of the data in these three runs where they overlap (runs 1 and 10 near phase 0.5 and runs 7 and 10 near phase 0.85), it is tempting to say they all represent a similar behavior in the system. Clearly, there was additional circumstellar material at these epochs.

TABLE 5
Difference Profile Emission Data

Image	Phase	Type A			Type B		
		EW	Velocity		EW	Velocity	
		Å	km s^{-1}		Å	km s^{-1}	
			CM[a]	B-star[b]		CM[a]	B-star[b]
01-026	0.361	1.15	-110	-69	...	...	...
01-068	0.733	1.18	-56	-110	...	...	...
01-134	0.455	...	...	...	0.35	-36	-21
01-134	0.455	...	...	...	0.55	-363	-348
01-176	0.180	0.81	+128	+177	0.33	-456	-407
02-008	0.754	1.10	-62	-116	0.15	+154	+100
02-029	0.424	0.39	+74	+99	0.28	-131	-106
02-041	0.466	...	...	...	0.15	-105	-93
02-041	0.466	...	...	...	0.23	+58	+70
02-047	0.500	...	...	...	0.09	+62	+62
02-047	0.500	...	...	...	0.21	-93	-93
02-078	0.826	0.90	-97	-145	0.27	+128	+80
02-109	0.162	0.38	+37	+83	0.13	-140	-94
02-111	0.168	0.44	+25	+72	0.09	-139	-92
02-113	0.174	0.50	+36	+84	0.14	-141	-93
02-118	0.209	0.97	+40	+92	0.17	-147	-95
03-002	0.815	1.02	-94	-144	...	...	...
03-017	0.891	0.35	-114	-149	...	...	...
03-027	0.249	1.22	+57	+111	0.21	-132	-78
03-036	0.300	1.25	+48	+100	0.20	-134	-83
03-055	0.608	0.98	-114	-148	0.30	+129	+96
03-071	0.659	1.25	-103	-148	0.36	+192	+147
05-009	0.494	...	...	...	0.15	+68	+70
05-009	0.494	...	...	...	0.19	-102	-100
05-069	0.860	0.35	-147	-189	...	...	...
05-090	0.202	0.67	+120	+171	0.26	-140	-88
05-096	0.222	0.68	+127	+180	0.36	-159	-106
05-102	0.242	0.72	+88	+142	0.20	-163	-109
05-108	0.261	0.68	+84	+138	0.19	-153	-99
05-116	0.274	0.64	+82	+135	0.23	-155	-102
05-150	0.578	0.49	-133	-159	0.17	+97	+72
05-252	0.288	0.67	+76	+129	0.21	-159	-107
05-310	0.656	0.85	-138	-183	0.16	+119	+75
05-311	0.661	0.85	-145	-191	0.19	+120	+74
05-313	0.668	0.80	-153	-200	0.21	+106	+59
06-022	0.185	0.67	+47	+97	0.18	-152	-103
06-025	0.196	0.68	+40	+91	0.19	-152	-101
07-075	0.764	0.71	-143	-197	0.86	+257	+203
07-077	0.768	0.74	-149	-203	0.82	+262	+208
07-123	0.073	...	...	...	0.10	+423	+447
07-123	0.073	...	...	...	0.42	-378	-354
07-190	0.800	0.95	-153	-204	0.96	+314	+262
07-196	0.821	0.53	-41	-90	0.55	+350	+302
07-198	0.838	0.39	-40	-86	0.08	+90	+44
07-198	0.838	...	...	...	0.46	+386	+340
07-200	0.844	0.27	-95	-140	0.13	+71	+26
07-200	0.844	...	...	...	0.49	+365	+321
07-325	0.889	0.09	-82	-117	0.19	+422	+387
08-037	0.306	1.33	+59	+110	0.11	-153	-102
08-039	0.317	1.06	+71	+121	0.15	-142	-93
08-045	0.325	1.07	+67	+115	0.16	-152	-104
08-109	0.681	0.99	-104	-153	...	...	...
08-225	0.392	0.62	+73	+107	0.12	-110	-76
08-272	0.753	0.78	-132	-186	...	...	...
08-273	0.758	0.78	-128	-182	...	...	...
08-325	0.107	0.34	+181	+215	...	...	...
09-024	0.190	0.97	+96	+147	0.20	-155	-104
09-066	0.555	...	...	...	0.19	+104	+86
09-066	0.555	...	...	...	0.24	-128	-146
09-122	0.257	0.72	+66	+120	0.14	-146	-92
09-180	0.625	0.68	-134	-172	0.21	+105	+67
10-049	0.831	0.86	-213	-260	0.75	+322	+275
10-098	0.187	0.81	+145	+195	0.25	-166	-116
10-015	0.463	...	...	...	0.19	-12	+1
10-015	0.463	...	...	...	0.22	+386	+399
10-015	0.463	...	...	...	0.70	-426	-414
10-104	0.207	0.75	+147	+199	0.26	-143	-91
10-140	0.542	...	...	...	0.22	-421	-435
10-140	0.542	...	...	...	0.68	-21	-35
11-124	0.675	1.22	-138	-187	...	...	...
11-129	0.685	1.26	-127	-177	...	...	...
11-138	0.697	1.28	-123	-174	...	...	...
11-239	0.398	0.72	+5	+37	...	...	...
11-282	0.753	0.82	-67	-121	...	...	...
11-283	0.759	0.76	-55	-109	...	...	...
11-293	0.769	0.72	-47	-101	...	...	...
11-294	0.774	0.68	-51	-104	...	...	...
11-296	0.780	0.67	-48	-101	...	...	...
11-297	0.785	0.67	-49	-102	...	...	...
12-005	0.900	0.06	-191	-223	...	...	...
12-039	0.340	1.06	+2	+47	0.23	-428	-382
03-105[c]	0.994	0.24	...	-25	...	...	...
03-107[c]	0.004	0.31	...	-25	...	...	...
05-360[c]	0.997	0.05	...	-149	0.06	...	+140
05-362[c]	0.002	0.06	...	-132	0.06	...	+110
05-364[c]	0.006	0.06	...	-121	0.06	...	+165

Notes: [a] System center-of-mass rest frame. [b] B-star rest frame. [c] During primary eclipse.

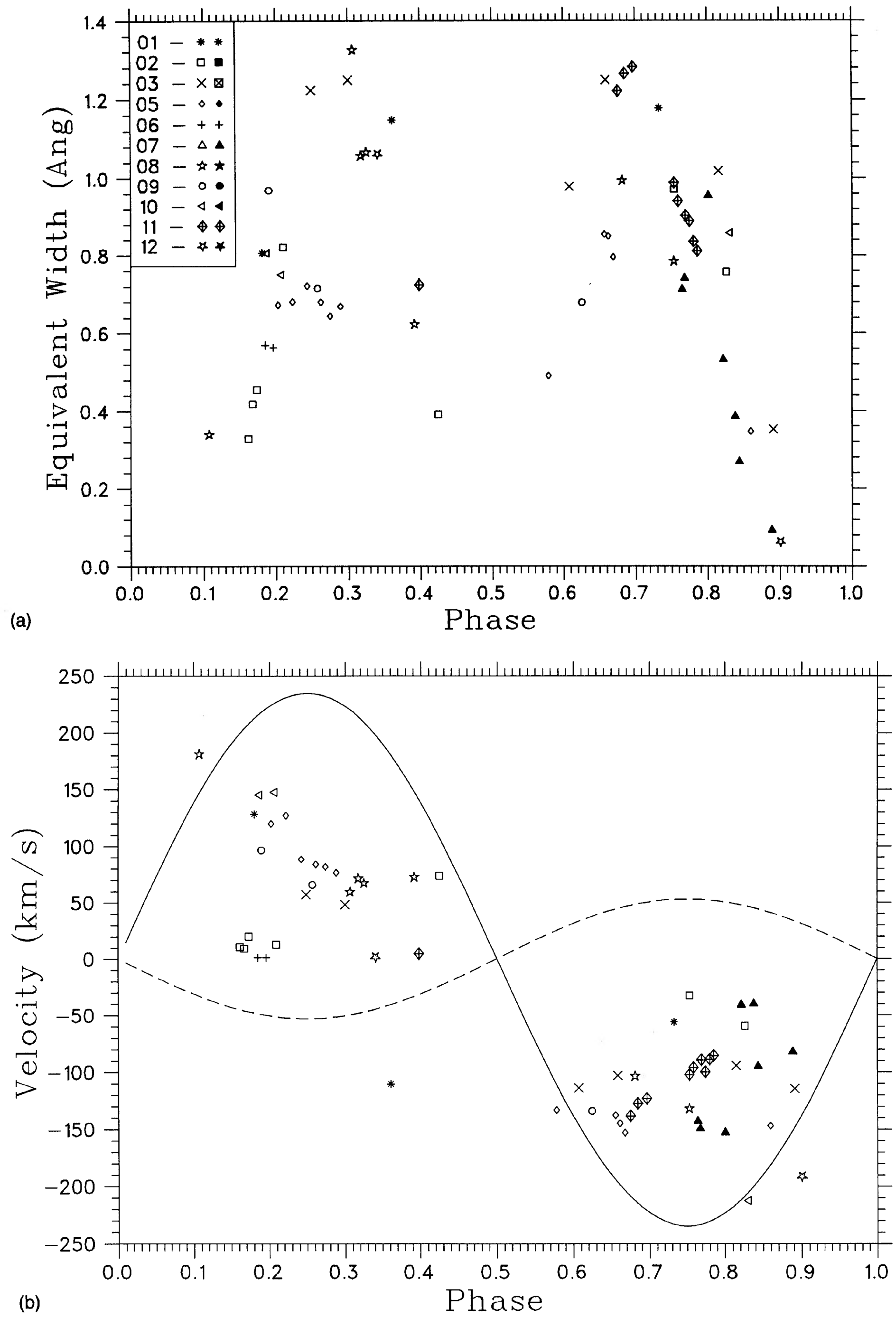

FIG. 4—(a) Type A emission equivalent widths vs. phase. The symbols correspond to different observing runs (see Table 2), and are marked in the upper left-hand corner of the figure. The second symbol denotes the weaker of a pair of emission components from one observation. (b) Type A emission radial velocities (in the CM frame) vs. phase. The symbols are as in (a). The radial velocity of the primary and secondary stars are depicted by a dashed line and a solid line, respectively.

5.3 In-Eclipse Profiles

The difference profiles from the five exposures in the totality of primary eclipse are displayed in Fig. 6. Observations 03-105 and 03-107 spanned the phase range 0.990–0.000 and 0.000–0.008, while the run 5 observations spanned the phase range 0.995–0.007 (covering 0.004 phase units each). The run 3 exposures show a single peak, while the run 5 exposures have two weaker peaks. The EW and radial velocities of these features are shown in Fig. 5 and listed at the end of Table 5. The EWs are with respect to the out-of-eclipse continuum, and the velocities are in the B-star rest frame. Note that often the weaker component of the run 5 data is at or below the limit of detection if the data had been taken out-of-eclipse.

1993PASP..105..731V

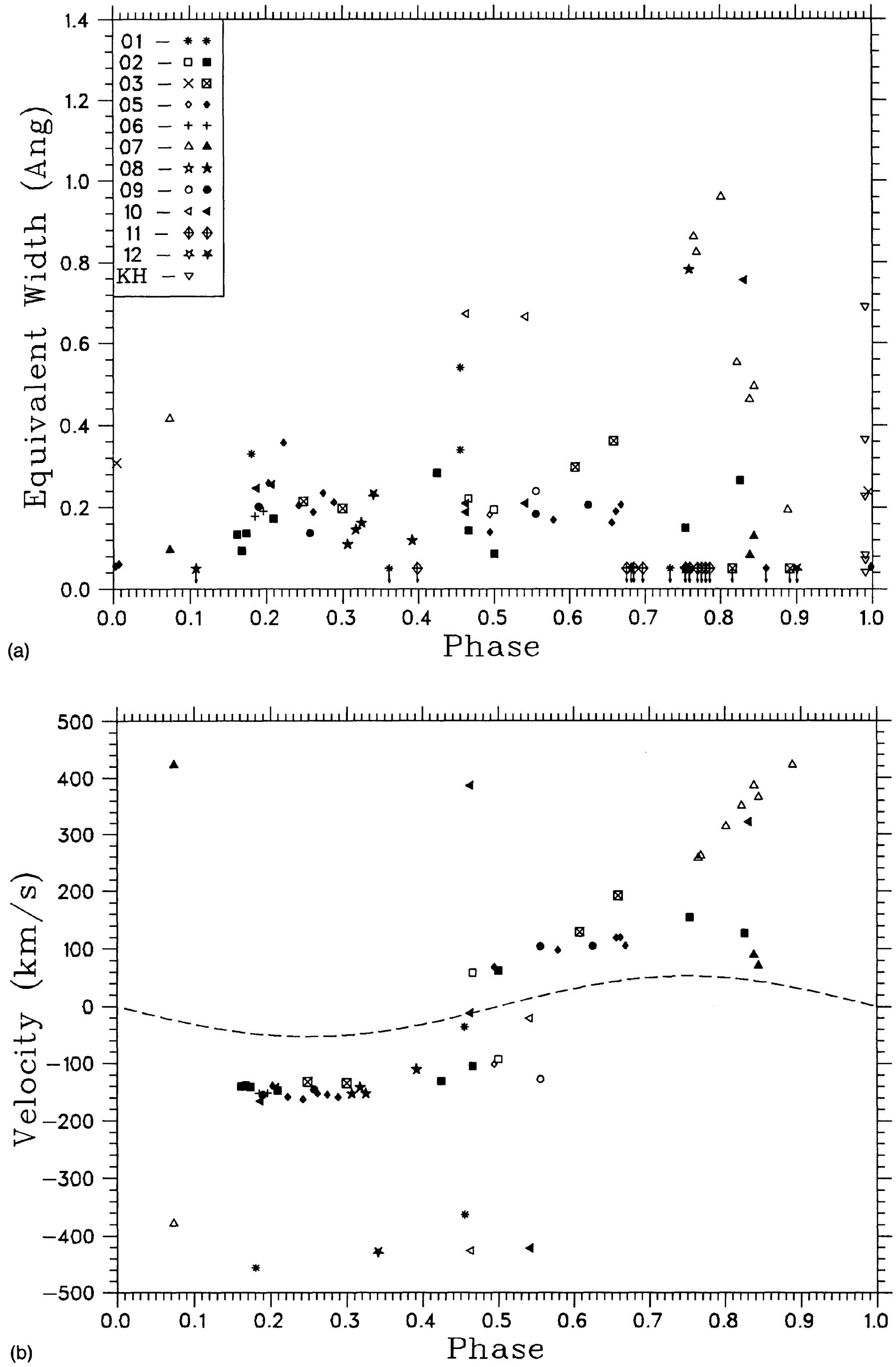

FIG. 5—(a) Type B emission equivalent widths vs. phase. The symbols correspond to different observing runs, and are marked in the upper left-hand corner of the figure. The second symbol denotes the weaker of a pair of emission components from one observation. KH refers to eclipse data from Kaitchuck and Honeycutt (1982). Symbols near EW=0.05 Å, with downward arrows superimposed, denote the lower limit of detection for observations where no Type B emission was detected. (b) Type B emission radial velocities (in the CM frame) vs. phase. The symbols are the same as in (a). The radial velocity of the B star is depicted by a dashed line.

The run 3 eclipse observations show a single, strong emission feature. The feature's EW matches the run 3 Type B emission EWs, but the in-eclipse velocity is much smaller. Since these exposures were entirely between second and third contact, and the secondary star is larger than the primary, the emission source (if in the orbital plane) cannot be between the stars or near the surface of the primary. If the emission source is on the surface of the secondary (presumably attributed to chromospheric/coronal activity), we might expect to see it in observations in the phase interval ~0.75–0.25. It would appear in the red-shifted wings of the Type A emission features of observations 03-027 and 03-036, and the blue-shifted wings of observations 03-002, 03-055, and 03-071. While we may

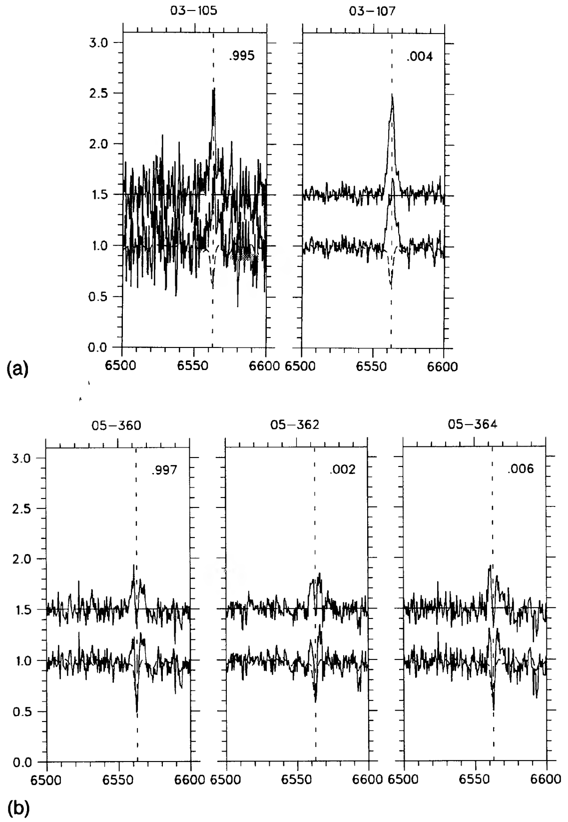

FIG. 6—(a) The in-eclipse spectra from run 3. The format is the same as that of Fig. 1, except that the difference profile continuum is shifted to 1.5 for clarity. The first observation was taken through clouds. (b) The in-eclipse spectra from run 5. The format is the same as that of (a).

speculate that these wings are wider during this run versus other runs, this is not conclusive. Of course, chromospheric features are transient. The in-eclipse spectra were taken on the last day of an observing run, and the only out-of-eclipse spectra that have visibility to the outer face of the secondary were taken at least three days earlier. It is possible that the feature appeared during this interval. Since Kaitchuck (1981) reported seeing at rest hydrogen emission during only one of 18 eclipses of RW Tau, this is probably not a common or long-lived feature.

A similar single-peaked feature was observed in U Cep by Kaitchuck et al. (1989). They observed six eclipses both photometrically and spectroscopically. During one eclipse they spectroscopically observed both trailing and leading accretion disk sides, plus a third emission component. This component was absent at mideclipse when the disk was totally eclipsed, but had a constant $\sim +100$ km s^{-1} velocity both before and after its eclipse. Kaitchuck et al. postulated that this could be gas escaping from the L_3 point. They had no out-of-eclipse data to confirm this.

At this point we can only speculate that the run 3 eclipse emission feature was a rare massive chromospheric flare. While interesting in its own right, this feature will shed little light on the nature of the out-of-eclipse emission.

The run 5 eclipse observations showed two small peaks, one red and one blue shifted from Hα. The eclipse EWs are only $\frac{1}{3}$ as strong as the Type B emission data, but the eclipse velocity matches that of the Type B data. Assuming the emission is associated with the primary star (possibly a ring or circumstellar bulge), then for both red- and blue-shifted emission to be visible, the width of the emission source must exceed that of the secondary star. We calculated that these observations were taken from phase 0.995 to 0.007, but recall there is some uncertainty in our ephemeris. For an observation at mideclipse, the emission source must extend at least 0.33 R_1 from each side of the primary to be visible. At any other phase of totality, one component of the emission source may be smaller, but then the other must be larger. We will return to this point in Sec. 8.5, where we compare the out-of-eclipse and in-eclipse spectra.

6. VISIBILITY AND VELOCITY INFORMATION

The variation of the visibility of the out-of-eclipse emission with phase can provide information about its location. In this section we will examine the visibility information with as few assumptions about the source of emission as possible. For this geometrical argument, we will assume that the only sources of opacity in the system are the stellar components. While a full radiative transfer analysis would be more accurate, our poor understanding of the nature of the circumstellar material precludes this. We will also assume that any emission source is largely confined to the orbital plane. Since the system's inclination is nearly 90° this reduces the analysis to a two-dimensional problem. For this discussion we define spinward as the direction of the system's rotation. A prograde velocity is a velocity in the spinward direction. We will assume that any emission source has a prograde (or at least nonretrograde) velocity. In Sec. 7 we explore possible sources of emission, and find that this is reasonable. This assumption will allow us to further restrict the locations of the emission sources. The net result is that a negative radial velocity places an emission source to the left of the CM of the system (as seen from that phase) and a positive velocity places it to the right of the CM of the system. Also, the minimum magnitude of the velocity increases linearly with an emission source's distance from the system CM.

6.1 Type A Emission Visibility and Velocity Information

As an example, we will examine the visibility and velocity information from the type A emission of run 9. Figure 7 is a scale model of RW Tau. Lines are drawn representing the limits of visibility from the edges of the silhouettes of the stars. These lines are tangent to the stellar surfaces, and parallel to a line from the system's center-of-mass (CM) to the position of the relevant phase on the outer circle. We have plotted the visibility information from four observations during run 9. The first two observations (09-024 and 09-122) are at phases 0.190 and 0.257. The EW decreases from 0.97 to 0.72 Å, indicating that emitting material was obscured between the phases. The radial velocities are $+96$ and $+66$ km s^{-1}, respectively. We have labeled the regions occupied by material bounded by the lines as 1, 2, 3, and 4. Since the velocities are positive, the condition of a prograde source eliminates region 1 from

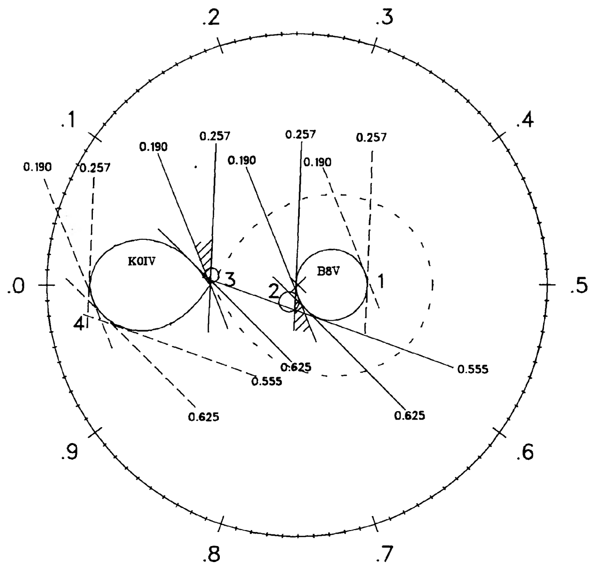

FIG. 7—The visibility limits for the Type A emissions in run 9. Each line is marked with the phase of the observation it represents. Spinward is CCW. The numbered regions are potential locations for the Type A emission. The circles in regions 2 and 3 represent candidate regions for the location of the Type A emission sources. See the text for further details.

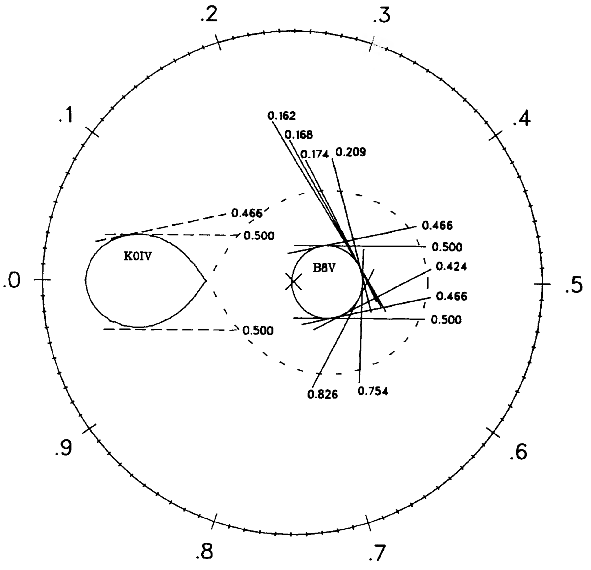

FIG. 8—The visibility limits for the Type B emissions in run 2. Each line is marked with the phase of the observation it represents. Note that observations near phase 0.5 have visibility limits on both stars. See the text for further details.

consideration. Region 4 is also eliminated, since the minimum radial velocity of a prograde source in this region is $\sim +325\ \mathrm{km\ s^{-1}}$ (for the observation at phase 0.257). Within the remaining regions, the decrease in EW between observations implies that material was obscured during this phase interval. The hatched areas show the obscured parts of the regions. The region 2 area was eclipsed by the B star. The region 3 area was "obscured" by changing from being projected on the sky to being projected on the K star. This requires that the emitting material is not much hotter than the K star (4270 K). This is not likely, but the region is included for completeness.

The second two observations (09-066 and 09-180) are at phases 0.555 and 0.625. The EW increased from 0.24 to 0.68 Å, and the radial velocities are -128 and $-134\ \mathrm{km\ s^{-1}}$, respectively. While observation 09-066 is of Type B emission, we include it because it is near the transition point between the Type A and B emission. Once again the velocities restrict the emission source for these observations to regions 2 and 3. Also, the EW increase implies that emitting material was exposed in the phase interval between the observations. For both regions 2 and 3 material is exposed from behind the B star. Combining the information from the four observations, we can restrict the potential emission sources to two reasonably well-defined locations. The potential source in region 2 is spinward from the line-of-centers. The potential source near region 3 is off-center in the opposite direction (antispinward).

Continuing with this technique, we can plot all the data from all the observing runs. The details will not be presented here. The results are all consistent with what has been presented in Fig. 7. We find that the temperature restriction on region 3 (that it must not be hotter than the K star) also applies to region 2 (this region must not be much hotter than the B star). While there is little reason to assume the hydrogen's temperature is less than the K star's, it is likely to be cooler than the B star's. This follows from the fact that hydrogen is almost completely ionized at 15,000 K. In any event, the Type A emission feature's location falls into one of two positions. It is either (a) a localized region $\sim 0.2\ R_1$ in radius, near the L_1 point, just antispinward of the line-of-centers (where R_1 is the radius of the primary star), with a temperature not greater than 4270 K or (b) a localized region $\sim 0.25\ R_1$ in radius, near the surface of the B star, just spinward of the line-of-centers, with a temperature not greater than 11,750 K. We have marked these regions on Fig. 7. These locations do not preclude features on the surfaces of the stars. Exceptions to these cases are runs 2, 3, and 8 where the emission lies closer to the line-of-centers, but is otherwise similar.

6.2 Type B Emission Visibility Information

Figure 8 has lines of visibility for all the Type B emission features in run 2. We have drawn just those lines that correspond to the correct doppler shift. By also examining Fig. 5, it seems clear that at this epoch the Type B emission source is extended and encircles at least 3/4 of the primary star. Plotting all the data from all the observing runs supports this conclusion. In runs 7 and 10 (and to a lesser extent 1) the Type B emission is exceptionally strong, but its location is consistent with the data from the other runs.

7. POTENTIAL SOURCES OF EMISSION

To make an accurate assessment of the emission's location, we need to fold in information about the physical nature and location of possible emission sources. In classic

Algols, the most obvious source of Hα emission is accretion structures resulting from mass loss from the secondary. Another is chromospheric activity on the late-type secondary star. Previous work on various Algol systems has already revealed the location of some Hα sources.

7.1 Theory and Models

Lubow and Shu (1975) performed semianalytic calculations of mass transfer in semidetached systems. They found that a narrow gas stream leaves the secondary's L_1 point. The Coriolis effect directs the stream towards the trailing side of the primary star, leaving the L_1 point at an angle of about 20° (for RW Tau) from the line-of-centers. The stream is somewhat collimated, having a scale width of $\sim 0.15\ R_1$ and a scale height (out of the plane of the orbit) of $\sim 0.10\ R_1$. Assuming there is no intervening material, we may expect the stream to be ionized by the primary star, much like an H II region.

In a system of RW Tau's dimensions, the stream will strike the facing side of the primary, approximately 45° around the star from the line-of-centers. The stream's velocity at impact is about $(2GM_1/R_1)^{1/2}$, or 560 km s^{-1} (with respect to the primary) for RW Tau. The sound speed $a_s = (kT/\mu m_H)^{1/2}$ for both the stream and the primary's photosphere/envelope is ~ 10 km s^{-1} (assuming $T = 10^4$ K for the stream and $\mu = 0.6$). Obviously, the stream's impact produces a strong shock, with a Mach number of ~ 56. If the ram pressure of the stream is less than the photospheric pressure, then the shock will be on the surface of the star. The photospheric pressure (P_0) at $\tau_{\rm ross} = 1$ was interpolated from Kurucz (1979) model atmospheres. Bilinear interpolation between Kurucz tabulated values gives $P_0 = 920$ dynes/cm^2 for $T_{\rm eff} = 11{,}750$ K, $\log(g_{\rm eff}) = 3.85$. The ram pressure is

$$P_{\rm ram} = \frac{\dot{M}}{a_s^2}\left(\frac{G^3 M_1^3}{32 R_1^7}\right)^{1/2} = P_0\left(\frac{10{,}000}{T}\right)\left(\frac{\dot{M}}{8 \times 10^{-11}}\right),$$

(Ulrich and Burger 1976) where the second equality assumes $\mu = 0.6$, M_1 and R_1 from Table 1, P_0 from above, and $\dot{M}$ in $M_\odot$ yr^{-1}. Obviously, $\dot{M}$ will have a great effect on whether or not the stream penetrates the photosphere. If the stream does not penetrate, we can expect to see the shock region. If it does penetrate, the shock may be "buried" in the primary's envelope, and will not be directly visible. Since the density profile across the stream is Gaussian it might be possible to "bury" the shock for the central part of the stream, leaving a visible shock in the less dense fringes. β Per has a mass-transfer rate of $\sim 10^{-10}\ M_\odot$ yr^{-1} (Richards 1992). Since its in-eclipse and out-of-eclipse emission is generally weaker than RW Tau's, we might expect that RW Tau's mass-transfer rate is larger (or at least not smaller) than β Per's at most epochs. If so, the shock should be buried. In that case the shock's energy would be released over a large area of the primary's surface, resulting in a larger $T_{\rm eff}$ in that region. The actual $T_{\rm eff}$ depends on the size of the region, which would depend on the shock depth, the stellar envelope's opacity and the rotation rate of the star. If the mass-transfer rate is large enough, and the gaining star rotates fast enough, then an equatorial bulge may form (Olson 1980). This occurs if the photon-diffusion time from the shock depth to the surface is greater than the time it takes for the equatorial material to circle the star. In this case the shock energy is released over the star's whole equator. Because the primary's rapid rotation gives the equator a low effective gravity, the photon pressure from the shock energy may cause an equatorial bulge. If the edge of the bulge is optically thin, there might be Hα emission at the edges of the stellar disk (where the bulge is projected against the sky). If the bulge is much cooler than the primary star, we would also expect to see absorption from the bulge region that is projected onto the B star.

So far we have assumed that all the mass in the stream reaches the shock region. A significant fraction of the stream can "bounce" (Prendergast and Taam 1974; Smak 1989). Given the low angle of impact, it seems quite possible that a significant fraction of the stream may travel past the impact region. If so, what would happen to this material? It does not possess enough energy to leave the system, so it should travel around the primary, eventually striking it again. This may form a so-called "transient disk" or ring (Kaitchuck et al. 1985). The material may accrete as it circles the star. Eventually, we would expect some material to completely circle the primary and strike the incoming stream. This would deflect the stream, as well as drive the ring material into the primary star. RW Tau's primary is too large to allow a classic accretion disk to form. For such a disk to be stable, it would need to orbit at about 0.85 R_1 (inside the primary) (Lubow and Shu 1975). We might expect material to build up behind the shock where the ring collides with the stream. Such material would be ionized by the shock and by radiation from the primary (and may block the stream from the primary's radiation). This may be visible at Hα.

The secondary (spectral type K0 IV) may be chromospherically active. This may result in Hα emission sources on the secondary's surface. These sources may last several orbits, but should not be stationary over several years.

In summary, from our knowledge of the physical nature of the system, we expect six regions to be candidates for Hα emission. (1) Parts of the stream may be ionized and emit like an H II region. (2) The stream's impact on the primary will produce a shock that may be visible at Hα. (3) If the mass-transfer rate and stellar rotation are large enough, the shock energy may be visible as an equatorial bulge. (4) Some of the stream material may bounce from the shock and form a ring. (5) A ring or bulge may cause a build-up of material where it impacts with the stream. This impact may also produce a visible shock. (6) Finally, chromospheric activity on the secondary may provide Hα emission. None of these regions would exhibit retrograde motion.

7.2 Previous Observations of Hα Emission

Observations of short-period Algols have already revealed some sources of Hα emission. Transient rings have been observed in several short-period Algols during primary eclipse (Kaitchuck et al. 1985). All these systems have dimensions that cause Lubow and Shu's (1975) gas stream to impact obliquely on the primary. In addition, KH did an extensive Hα and Hβ in-eclipse study of the ring in RW Tau. They detected a ring during 12 of 18 eclipses. The ring had a typical radius of $\sim 1.5\ R_1$ on the trailing side, and $\sim 1.2\ R_1$ on the leading side. The Hα emission had an EW of 0.05–0.69 Å at second contact (scaled to the out-of-eclipse continuum), with most of the observations at the lower end of this range. Hβ observations at eclipse showed radial velocities $\pm \sim 350$ km s^{-1} near second and third contact (prograde with respect to system rotation). Most features vary between observations, leading to the conclusion that the ring is never stable.

Both Gillet et al. (1989) and Richards (1992,1993) have observed out-of-eclipse Hα emission in β Per. Gillet et al. modeled the emission as the ionized portion of the stream (extending from the L_1 point to near the surface of the primary), and the hot spot where the deflected stream material reimpacts with Algol's primary. They found no evidence of a ring. Richards modeled the emission with a ring, a high-velocity rotating region within the ring, and a "localized region" of material near the primary, on the line-of-centers. She proposed that this latter material is the accumulation of the ring material behind the stream.

Olson (1980) observed an ultraviolet excess during the primary eclipse of U Cephei. He interpreted this as a circumstellar bulge (Sec. 7.1). Similar observations were reported for RW Tau (Olson 1982). There he deduced a 10,000 K, moderately UV-optically thick disk with large vertical thickness. The disk had a derived mass of $\sim 5\times10^{-12}\ M_\odot$ at one epoch. This "disk" was very similar to the bulges seen in U Cep. If the primary is rotating faster than synchronous speeds (as is the case for RW Tau), this bulge may also produce a build-up of mass behind the stream impact location, resulting in a "localized region" much as if there were a ring.

8. DISCUSSION

8.1 Stream Opacity

Before discussing the possible emission sources, it is worthwhile to investigate the opacity of the stream. If the stream is optically thick in the Hα line or the continuum near Hα the visibility of the Type A emission may be affected by the stream opacity. Hydrogen and helium bound–free and free–free opacities can be calculated using the stream densities from Lubow and Shu (1975). We assume $T=10{,}000$ K, noting that the opacities are not very T dependent. If $\dot{M}\geqslant 6.4\times10^{-5}\ M_\odot\ \mathrm{yr}^{-1}$, the opacity is dominated by the hydrogen bound–free process and the continuum opacity at Hα is $\tau\approx\dot{M}/10^{-9}$. As noted earlier, for β Per $\dot{M}\approx 10^{-10}\ M_\odot\ \mathrm{yr}^{-1}$. The mass-transfer activity level in β Per is somewhat below that of RW Tau. Therefore we may estimate that RW Tau's mass-transfer rate varies from below to above $10^{-9}\ M_\odot\ \mathrm{yr}^{-1}$, so the stream's continuum at Hα may be optically thick or thin at a given epoch. We might expect the stream to be thick during runs 1, 7, and 10, where the Type B emission strength suggests that mass-transfer activity is at a high level. Unfortunately, in those runs there are no observations near both phases 0.25 and 0.75 to compare. Still, the stream's continuum opacity might affect the results discussed below. The stream's Hα line opacity is visible in observations near primary eclipse. While this may affect the discussion below, an examination of the difference profiles in Fig. 3 shows that it does not seem strong at other phases.

8.2 Type A Emission Candidates

The visibility and velocity information gave two possible candidates for the Type A emission source location (see Fig. 7 and Sec. 6.1). The first candidate region is near the L_1 point. To fit the observed data, the region extends ~ 0.4 R_1 antispinward in the plane of rotation. Recall that the stream leaves the L_1 point angled spinward; we might therefore expect to see an emission source spinward of the L_1 point. But there is no reason to expect circumstellar material and hence emission in the opposite direction. While some of the Type A emission data has velocities similar to the L_1 point's synchronous rotation velocity of 140 km s^{-1}, most does not. In addition, this region has difficulties matching the visibility information for all the observations. Finally, this region required the emission source to not be hotter than the K star (4270 K). We conclude that this region is not the location of the Type A emission.

The second candidate region is near the surface of the primary star, just spinward of the line-of-centers. Lubow and Shu's (1975) calculations place the shock region from the stream/star impact too far spinward to be this source. Richards' (1992) "localized region" (the build up of material behind the stream where circling ring or bulge material hits the incoming stream) and the shock region in front of it are good candidates. In this case, the visibility of an emission source in this region should be affected by the stream's opacity.

8.3 The Type A Emission Region

We can examine the Type A emission EWs for signs of the stream's opacity. During periods of increased mass transfer (and hence high stream opacity) we would expect the EWs in the phase interval 0.5–1.0 to be smaller than those from the same epoch in the phase interval 0.0–0.5. In Fig. 4(a) the run 8 data suggests that the source is partially blocked during the 0.5–1.0 phase interval. However, runs 1, 2, 3, 5, and 10 show either a constant or stronger EW in the latter phase interval. Either we have misjudged the stream's opacity, or the Type A emission source is on both sides of the stream, or the Type A emission source's vertical extent allows equal visibility from both sides of the system. This could be the case if the shock region from the star/stream impact was the Type A emission source.

If the source is optically thin, then an observation at one phase will yield an identical EW and radial velocity to a simultaneous observation from the opposite side of the system (excepting the reversal of doppler shifts). Figure 9

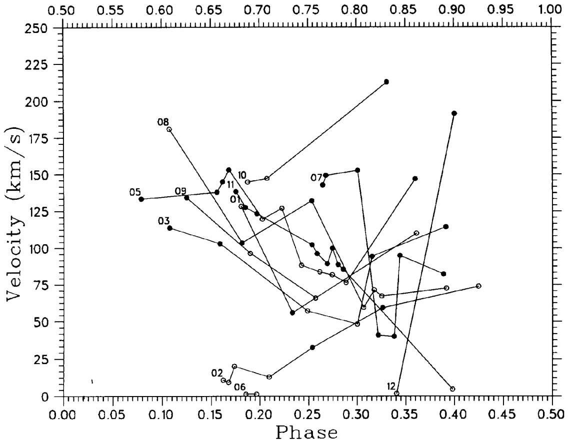

FIG. 9—The Type A emission radial velocities, with data overplotted for the 0.0–0.5 and 0.5–1.0 phase intervals (see the text). Open circles indicate data in the phase interval 0.0–0.5; closed circles for 0.5–1.0. The data for each run are connected by lines, with the number of each run placed to the left of the left-most data point.

shows the velocity data folded on the 0.0–0.5 phase interval. This plot also reduces undersampling in the data, to help find trends in the phase-dependent behavior of the velocities.

The data can be grouped into two cases. For most of the runs (1, 3, 5, 8, 9, and 11) the velocities start at 110–180 km s^{-1} at phase 0.15 and drop linearly to around 75 km s^{-1} at phase 0.4. Runs 2 and 6 have velocities $\sim$10 km s^{-1} at phase 0.15, which (for run 2) increase to 75 km s^{-1} by phase 0.3. Near phase 0.20 this velocity equals the synchronous rotation speed of the surface of the primary along the line-of-centers. This implies the emission source is nearly at rest on the surface of the B star. The variations in velocity might be due to the variations in the visible portion of the Type A emission source with phase. Of course, it is interesting that both these runs are also the only ones for which the EWs and radial velocities were calculated by Gaussian fits. However, calculating these velocities by direct integration just has the effect of adding $\sim$30 km s^{-1} to the magnitude of the Type A emission. While this makes these two runs' velocities closer to the values for the other observing runs, they are still much lower and peak at later phases. Clearly this represents a fundamentally different situation than the other runs.

In summary, we have two basic behaviors for the Type A emission. For most of the runs, the velocity magnitudes peak at 140 km s^{-1} near phase 0.17 (0.67). This is consistent with the visibility information's placement of the Type A emission near the surface of the primary, just spinward of the line-of-centers. For runs 2 and 6, the visibility information places the Type A emission source nearer to the line-of-centers. These velocities peak near phase 0.30, with a magnitude of $\sim$75 km s^{-1}. This places the Type A emission source almost at rest on the B star. Run 8 is also slightly nearer to the line-of-centers. We will return to this point in Sec. 8.7. Several runs have insufficient phase coverage for us to say conclusively that they match one of these two patterns; but we can say their behaviors are consistent with one of the two. Both these cases locate the type A emission source closer to the line-of-centers than the expected location of the star/stream impact location. However, there is little evidence that the stream's opacity affects the Type A emission.

8.4 Type B Emission Candidates

Visibility information shows the Type B emission source to surround the B star. KH's transient rings and/or Olson's (1980) equatorial bulge seem good candidates for this emission. If the type B emission source is a transient ring, then the Type B data should compare well with the transient ring data taken near second and third contact. This is especially true of Type B emission data obtained at phases 0.4901 and 0.5099 (second and third contact of the secondary eclipse). The EWs of the transient rings are shown in Fig. 5. The transient ring and Type B emission EWs are in the same range, especially if one notes that the lower range of the in-eclipse (ring) EWs are below the detection limits of our out-of-eclipse observations. The radial velocities are not so well correlated. The ring Hβ velocities at second contact were $\pm\sim$350 km s^{-1}, about three times the most commonly observed Type B emission velocities. However, one set of Hα radial velocities observed by Kaitchuck (1981) were lower ($\pm\sim$260 km s^{-1}). The Hα data were taken almost a year earlier than the Hβ data. It is not clear how the change from Hβ to Hα should change the observed velocities; we conclude that the change was in the velocity field of the ring. The present survey is 7+ years after the transient ring observations and there is no reason to rule out further change in the velocity field. However, runs 1, 7, and 10 show velocities that are consistent with the observed transient rings. Two of these runs (1 and 10) also have data near phase 0.5 that shows material nearly at rest with respect to the B star; these may be build-ups of ring material. In any event, it seems likely the Type B emission from runs 1, 7, and 10 arose from a transient ring.

For the other runs, a possible emission source is an equatorial bulge (Olson 1980). While the bulge itself is optically thick in the continuum, its outer region may be optically thin and visible at Hα. The Type B emission rotates at $\sim$100 km s^{-1} and the B star rotates at 94 km s^{-1}. To within the errors, these velocities are identical, which places the Type B emission on the surface of the B star. Unfortunately, Olson's calculations of the bulge for U Cep imply that RW Tau's primary rotates too slowly to form an equatorial bulge. However, Olson has observed the same continuum UV excess in RW Tau as he saw in U Cep (Olson 1982). We can only say the Type B emission velocity and visibility information place it on the surface of the B star, ringing the equator. Given that, we may envision a similar process to Olson's bulge formation that leads to the Type B emission at most epochs.

8.5 Comparison with In-Eclipse Data from This Survey

A useful comparison would be to obtain observations of an eclipse during the current survey. We would expect the spectrum at second and third contact to match that of a Type B emission spectrum. Unfortunately, a string of weather and instrument problems, as well as a changing orbital period, have frustrated our attempts to gather this data. As described in Sec. 5.3, we currently have data from only two eclipses, during runs 3 and 5. Since these observations cover mideclipse to third contact, we should be able to compare them with both our out-of-eclipse data and KH's in-eclipse observations. Since the telescope used for this survey is smaller than the one used for KH's transient ring examination, the phase resolution is coarser. However, the spectral resolution is higher.

Recall that the observations from run 3 were dominated by what is apparently a rare massive flare. Such events cannot explain the Type B emissions that have been somewhat constant over four years. The observations from run 5 are more useful. They have two emission components, both with EWs smaller than the typical Type B EWs, but with radial velocities that compared well with the Type B velocities in the B star's frame. This is consistent with a circumstellar bulge. However, both red- and blue-shifted features were visible from mideclipse to third contact. This implies that both emission component sources extended at least $\sim 0.33\ R_1$ from the primary star at mideclipse, and the red component extended at least $\sim 0.66\ R_1$ at third contact. It is hard to envision a bulge of this extent, and we are left assuming we are seeing a slowly rotating ring (SRR). This ring has radial velocities $\frac{1}{2}$–$\frac{1}{3}$rd that of KH's transient rings (see Sec. 8.4). We will refer to KH's transient rings as rapidly rotating rings (RRRs). We cannot probe the SRR structure as KH did for the RRR, as we have neither their phase resolution nor phase coverage.

To further compare our observations with KH's, we convolved our spectra to match their lower spectral resolution. For data convolved to match KH's KPNO data (spectral resolution 2.5 Å), the emission lines are still quite visible. While the two emission components require deblending to extract the EWs and velocities, the values obtained are not significantly different from the values listed in Table 5. Convolving our data to match KH's Goethe Link Observatory spectral resolution (~ 8 Å) reduces the emission to a barely detectable, single, broad, low peak. With any noise in the data, the feature would be hard to detect.

Our in-eclipse observations compare well with the four faintest KH emission detections. These detections were all observed from Goethe Link Observatory at Hα. Because of the emission's faintness, KH co-added all the spectra in each eclipse to examine the data. The co-added emission EWs were ~ 0.042–0.084 Å and the FWHMs were generally less than 380 km s^{-1} (once again, we have scaled all the EWs to the out-of-eclipse continuum). These match the values for our smoothed SRR observations. Information about the emission's velocity was lost in the co-adding process. It is tempting to suggest that the fainter emission KH detected was not from RRRs like the ring they examined is great detail, but rather that the fainter emission may be from an SRR like the one we observed during the run 3 eclipse. This division of KH's emission sources matches the division in the Type B data. Runs where the Type B EW was $\lesssim 0.4$ Å had velocities around 100 km s^{-1} (B-star frame), while those runs (1, 7, and 10) with higher EWs (up to 1 Å) also had the higher RRR velocities.

8.6 Type B Emission Prevalence

Another comparison of the Type B emission with the transient rings and bulges is the frequency of detection. As discussed above, transient rings (RRRs) were detected 66% of the time. Olson (1982) observed distortions in RW Tau's eclipse light curve during five of nine eclipses (56% of the time). Table 5 and Fig. 5 show that Type B emission was observed in 10 of 11 observing runs. Of the ten, three (runs 1, 3, and 8) did not show Type B emission at all phases. The nondetections were clustered around phase 0.75, and may be explained by a build-up of optically thick material just spinward of the stream impact point. For the run where no Type B emission was detected (run 11), the width of the emission suggests that the Type B emission source exists, but its emission is blended with the Type A emission. If true, then the frequency of the Type B emission (100%) is much higher than that of the transient rings (66%) or bulges (56%). However, recall that the emission KH observed in four of their twelve ring detections may have been from an SRR. In addition, in five of the six eclipses where KH detected no emission, their lower limit of detection is higher than the EW we observed for the SRR. So for the 18 eclipses KH observed, an SRR may have been present in nine of them. Of the remaining nine, eight eclipses had RRRs. The picture that emerges is that from 1978 to 1981 (during the Kaitchuck and Honeycutt, and Olson observations) an RRR was present 44% of the time, while an SRR may have been present $\sim$20%–60% of the time. From 1988–1992 (during the current survey) an RRR was present 27% of the time (during runs 1, 7, and 10), with an SRR present during all the remaining time.

8.7 Type A and Type B Line-of-Sight Overlap

One unfortunate feature of our interpretation of the location of the emission features is that some of the Type B emission source material shares each line-of-sight to the Type A emission source. This is usually not a problem, since the Type B emission is much weaker than Type A. However, for runs 7 and 10 the Type B emission EWs are as strong as the Type A features. This blurs the distinction between the two. For these runs we must interpret the velocities and EWs of the Type A emission as representative of both the "real" Type A emission source and the Type B material around it. As such, the visibility information will place the Type A emission as arising much closer to the line-of-centers than its real location. However, the run 8 Type A emission is also closer to the line-of-centers, despite its lower Type B emission strength.

9. CONCLUSION

We have identified two primary out-of-eclipse Hα emission sources in RW Tau. The variation of EWs and radial velocities with phase allow us to locate these sources in the system. The Type A emission arises in a region $\sim 0.25\ R_1$ in radius, near the surface of the B star. In nine of eleven runs it is located somewhat spinward from the line-of-centers, and has a velocity magnitude of $\sim 140\ \mathrm{km\ s^{-1}}$. This region shows little sign of being eclipsed by the stream material. Depending on the opacity of the stream, we can identify two possible sources for this emission:

(A) If the stream is optically thick, then the Type A emission source must have a vertical extent that allows it to be equally visible from both phase 0.25 and phase 0.75. A good candidate is the star/stream impact shock region. This region may extend outside the diameter of the stream, allowing the required vertical extent. However, Lubow and Shu's (1975) calculations show the star/stream impact point is too far spinward to be the Type A emission region. Some process must consistently steer the stream against the Coriolis force for this case to hold.

(B) If the stream is optically thin, Richards' (1992a) Localized Region (of gas that builds up where rotating ring material intersects the incoming stream material) is a good candidate. This would be located between the star/stream impact region and the line-of-centers, matching that of the Type A emission. However, our calculations in Sec. 8.1 shows that at some epochs the stream should be optically thick. For his case to hold, we must have misjudged the stream's opacity.

For the remaining two runs, the Type A emission region is closer to the line-of-centers, and has a velocity magnitude of $\sim 10\ \mathrm{km\ s^{-1}}$ (approximately the synchronous velocity of the B-star's surface). We can only speculate at the origin of the Type A emission during these runs, but its near-Gaussian line profile suggests a compact, uniform source. One possibility is that magnetic activity at the L_1 point deflected the gas stream so that it impacts nearer to the line-of-centers. The more direct impact may result in less stream material bouncing from the impact, and hence allow clearer visibility to this region.

The Type B emission source is extended and surrounds the B star. For 8 of 11 observing runs its radial velocity is approximately that of the rotational velocity of the B star. One in-eclipse observation series shows an emission source whose EW and radial velocity are consistent with the Type B source. The in-eclipse emission source must have a radial extent of at least 0.33–0.66 R_1. If our in-eclipse emission source is the same as the Type B emission source, then the Type B emission must arise in a slowly rotating ring of material around the B star. This ring is at least as large as the transient rings of KH, but has a lower EW and lower radial velocities. It is proposed that several of the weaker rings observed by KH are actually of this slowly rotating material. During three observing runs, the Type B emission shows EWs and radial velocities consistent with KH's rapidly rotating transient rings. During the two runs where the Type A emission shows anomalous behavior, the Type B emission shows its most common (slowly rotating) state.

The reduction of all out-of-eclipse emission behavior to two categories is simplistic and there may be several circumstellar sources. Still, this picture is a useful initial discussion of the circumstellar material in the system. Because our observations cover several years, we have some information on the secular behavior of this system. We have described both a most "common" behavior and noted some unexplained variations. The results for RW Tau may or may not be representative of short-period Algol systems. RW Tau has a history of above-average emission activity. The analysis of other systems (in progress) should help us properly judge whether the RW Tau accretion structures deduced here have broad significance.

It is our pleasure to thank the staff of the U.S. Naval Observatory, Flagstaff Station for their help in setting up our observing runs. In particular, Jeff Pier has been most helpful. We would also like to thank John Jurcevic, Tom Hunt, Jeff Pier, Jeff Robertson, Jay White, and Tae Yoon for helping collect some of these observations. This research has made use of the SIMBAD database, operated at CDS, Strasbourg, France, and the IRAF software package, produced by NOAO. This work was supported by the National Science Foundation.

REFERENCES

Batten, A. H., Fletcher, J. M., and MacCarthy, D. G. 1989, Eighth Catalogue of the Orbital Elements of Spectroscopic Binary Systems (Victoria, B. C., Dominion Astrophysical Observatory)

Chambliss, C. R. 1992, PASP, 104, 663

Frieboes-Conde, H., and Herczeg, T. 1973, A&AS, 12, 1

Gillet, D., Mouchet, M., and North, P. 1989, A&A, 219, 219

Gunn, J. E., and Stryker, L. L. 1983, ApJS, 52, 121

Gray, D. F. 1976, The Observation and Analysis of Stellar Photospheres (New York, Wiley)

Grygar, J., Cooper, M. L., and Jurkevich, I. 1972, Bull. Astron. Inst. Czechoslovakia, 23, 147

Hanžl, D. 1990, Inf. Bull. Var. Stars, 3423

Honeycutt, R. K., Vesper, D., White, J., Turner, G. W., and Adams, B. 1990, in CCDs in Astronomy II: New Methods and Applications of CCD Technology, ed. A. G. D. Philip, D. S. Hayes, and S. J. Adelman (Schenectady, L. Davis), p. 177

Honeycutt, R. K., and Turner, G. W. 1993, in Robotic Telescopes in the 1990s, ed. A. Filippenko (San Francisco, ASP Series), p .77

Honeycutt, R. K., Vesper, D. N., Yoon, T. S., and White J. C., 1993, in Proceedings from the Pacific Rim Colloquium on New Frontiers in Binary Star Research, Seoul, ed. K.-C. Leung (San Francisco, ASP Series), p. 343

Joy, A. H. 1942, PASP, 54, 35

Kaitchuck, R. K. 1981, PhD Thesis, Indiana University

Kaitchuck, R. K., Honeycutt, R. K., and Faulkner, R. D. 1989, ApJ, 339, 420

Kaitchuck, R. H., and Honeycutt, R. K. 1982, ApJ, 258, 224 (KH)

Kaitchuck, R. H., Honeycutt, R. K., and Schlegel, E. M. 1985, PASP, 97, 1178

Kholopov, P. N., ed. 1985, General Catalogue of Variable Stars, 4th ed. (Moscow, Nauka)

Kurucz, R. L. 1979, ApJS, 40, 1
Lubow, S. H., and Shu, F. H. 1975, ApJ, 198, 383
Olson, E. C. 1980, ApJ, 241, 257
Olson, E. C. 1982, ApJ, 259, 702
Peters, G. J. 1989, Space Sci. Rev., 50, 9
Plavec, M. J., and Dobias, J. J. 1983, ApJ, 272, 206
Plavec, M. J., and Polidan, R. S. 1976 in Structure and Evolution of Close Binary Systems, ed. P. Eggleton, S. Mitton, and J. Whelan (Dordrecht, D. Reidel), p. 289
Prendergast, K. H., and Taam, R. E. 1974, ApJ, 189, 125
Richards, M. T. 1992, ApJ, 387, 329
Richards, M. T. 1993, ApJS, 86, 255
Smak, J. 1989, Space Sci. Rev., 50, 109
Struve, O., and Sahade, J. 1956, PASP, 69, 41
Struve, O., Sahade, J., and Huang, S.-S. 1957, PASP, 69, 342
Terrell, D., Mukherjee, J. D., and Wilson, R. E. 1992, Binary Stars, A Picture Book (Malabar, FL, Krieger)
Ulrich, R. K., and Burger, H. L. 1976, ApJ, 206, 509
Van Hamme, W., and Wilson, R. E. 1990, AJ, 100, 1981